Radar-derived Quantitative Precipitation Estimation in Complex Terrain over the Eastern Tibetan Plateau

Yabin Gou[a,b], Yingzhao Ma[c,d], Haonan Chen[e,f], Yixin Wen[g,h]

[a]*Hangzhou Meteorological Bureau, Hangzhou 310051, China*

[b]*Zhejiang Institute of Meteorological Sciences, Hangzhou 321000, China*

[c]*Department of Civil and Environmental Engineering, The Hong Kong University of Science and Technology, Hong Kong SAR 999077, China*

[d]*State Key Laboratory of Hydro-science and Engineering, Department of Hydraulic Engineering, Tsinghua University, Beijing 100084, China*

[e]*Colorado State University, Fort Collins, CO 80523, USA*

[f]*NOAA/Earth System Research Laboratory, Boulder, CO 80305, USA*

[g]*Cooperative Institute for Mesoscale Meteorological Studies, University of Oklahoma, Norman, OK 73019, USA*

[h]*NOAA/National Severe Storms Laboratory, Norman, OK 73072, USA*

Revised Manuscript Submitted to *Atmospheric Research*

October 2017

Corresponding author address: *Haonan Chen, 1373 Campus Delivery, Colorado State University, CO 80523. E-mail: Haonan.Chen@colostate.edu*

Abstract

Quantitative Precipitation Estimation (QPE) is one of the important applications of weather radars. However, in complex terrain such as Tibetan Plateau, it is a challenging task to obtain an optimal *Z-R* relation due to the complex spatial and temporal variability in precipitation microphysics. This paper develops two radar QPE schemes respectively based on Reflectivity Threshold (RT) and Storm Cell Identification and Tracking (SCIT) algorithms using observations from 11 Doppler weather radars and 3264 rain gauges over the Eastern Tibetan Plateau (ETP). These two QPE methodologies are evaluated extensively using four precipitation events that are characterized by different meteorological features. Precipitation characteristics of independent storm cells associated with these four events, as well as the storm-scale differences, are investigated using short-term vertical profile of reflectivity (VPR) clusters. Evaluation results show that the SCIT-based rainfall approach performs better than the simple RT-based method for all precipitation events in terms of score comparison using validation gauge measurements as references. It is also found that the SCIT-based approach can effectively mitigate the local error of radar QPE and represent the precipitation spatiotemporal variability better than the RT-based scheme.

Keywords: Weather Radar, Quantitative Precipitation Estimation (QPE), Reflectivity Threshold, Storm Tracking/Identification, Complex Terrain, Tibetan Plateau

1. Introduction

Radar quantitative precipitation estimation (QPE) is an active and vibrant field with numerous accomplishments resulting in practical applications such as worldwide deployment of weather radars and urban scale flood application of dense radar networks (e.g., Yoshikawa et al., 2012; Chen and Chandrasekar, 2015; Shimamura et al., 2016; Chandrasekar et al., 2018). However, fundamental challenges in radar QPE still exist from both physical science and radar engineering points of view (Cifelli and Chandrasekar, 2010). On the one hand, the performance of radar QPE greatly relies on the physical model of raindrop size distribution (DSD) and the relation of the physical model to radar parameters. The precipitation microphysics in different storms or different regimes within a single storm cell may vary due to the complex internal cloud microphysical processes and/or external environmental factors (Chapon et al., 2008; Lee et al., 2005; Smith et al., 2009; Yoshikawa et al., 2014). As a result, the inherent errors associated with the radar reflectivity and rainfall rate relationships (i.e., Z–R relations) derived for such nouniformly distributed precipitation are difficult to remove (Bringi and Chandrasekar, 2001; Steiner and Smith, 2000; Cifelli and Chandrasekar, 2010). On the other hand, the system engineering issues including radar measurement height, beam broadening, and coverage limitations also pose challenges to radar QPE (Fulton et al., 1998; Chen and Chandrasekar 2015). Such engineering challenges are especially obvious in operational or urban environments (Chandrasekar et al., 2018; Cifelli et al., 2018). Both the physical and engineering considerations make it difficult to find an ideal Z-R relation that is able to capture the spatial and temporal variability of precipitation in different storm seasons for a certain region.

A large number of previous studies have been devoted to improving radar QPE using precipitation measurements from rain gauges. The regional precipitation climatology derived using long-term radar and gauge observations is a useful tool to guide the development of radar rainfall products (Crochet, 2009; Nesbitt et al., 2006). Rain gauge data are also commonly used to conduct radar QPE mean-field-bias correction (e.g., Seo et al., 1999) and local bias correction (e.g., Zhang et al., 2016; Willie et al., 2017). However, most of the previous research focused on single *Z-R* relation-based analysis, which is not enough since different rain types may coexist especially in large-scale precipitation systems such as typhoon and Meiyu Front in China (Gou et al, 2014). In recent years, different empirical *Z-R* relations are used for different surface precipitation types such as stratiform or convective rain. Typical examples include the multi-radar multi-sensor (MRMS) system developed by Zhang et al. (2016), which adopts different *Z-R* relations for warm/cool stratiform rain and convective rain and hail. In addition, dense radar-gauge pairs may supply very useful feedback information for the quantitative reconstruction of *Z-R* relationships (Alfieri et al, 2010).

In complex terrains such as Northern California (Willie et al., 2017; Cifelli et al., 2018) or Tibetan Plateau (TP), the selection of appropriate *Z-R* relation is more challenging due to additional environment factors such as partial beam blockage (PBB) and bright-band (BB) contamination (Kitchen et al., 1994; Fulton et al., 1998; Willie et al., 2016). The orographic enhancement in complex terrain also has significant impacts on regional rainfall climatology (White et al. 2003). In this paper, a network of 11 Doppler weather radars and a dense rain gauge network over the Eastern Tibetan Plateau (ETP) are used to demonstrate radar rainfall performance in this complex terrain typically influenced by its unique topography and climate. Two adaptive QPE schemes are developed to dynamically reconstruct radar rainfall relations by fitting real-time radar-gauge rainfall observations using probability matching method (PMM: Rosenfeld et al., 1994). One is based on reflectivity threshold (RT), which assumes that similar radar echoes are homogeneous and fitting of

Z–R relationship is done at every 5 dBZ intervals. The other one is based on the SCIT algorithm (Johnson et al. 1998) that refines three-dimensional multi-radar mosaic grids into independent storm regions to capture storm-scale or regional precipitation features (Gou et al., 2015). The microphysical principles of these two QPE schemes, their representative capability in convective conditions induced by orographic enhancement, as well as their rainfall performance over such a complex terrain are detailed in this paper. In addition, the ground radar based storm-scale VPR is investigated to reveal the microphysical differences between storm cells.

The main goal of this study is to address the aforementioned issues regarding the SCIT-based approach based on four precipitation events over the ETP. Section 2 introduces the datasets and QPE methods. Section 3 details the precipitation events used for evaluation and their microphysical differences during the storm evolutions through investigating the storm-scale VPRs. The evaluation results of the RT and SCIT based QPE algorithms are presented in section 4. Section 5 summarizes the main points of this paper and suggests directions for future research.

2. Data and methodology

2.1. Study area

The ETP is located near the Hengduan Mountains, Southwest of China. Fig. 1 illustrates the digital elevation map (DEM) of China and particularly for this study domain（102°E–111°E, 28°N–33°N). Fig. 1b shows that the region of interest in this study extends from Hengduan Mountains to Wushan Mountains to the east, Ta-pa Mountains to the north, Dalou Mountains to the southeast, and the Yunnan-Guizhou Plateau to the southwest. It covers over 260,000 km^2 in total with an average elevation surpassing 4000 m above mean sea level (MSL) in the west, 3000 m above MSL in the north, and 2000 m above MSL in the south. The ETP exerts a direct influence on the social and economic development in this region, due to its multiple climatic systems, complex geomorphology, and various internal and external geological and ecological impacts. The ETP is characterized by the unique interactions among the atmosphere, hydrosphere, and biosphere. In particular, special atmospheric and active hydrological processes occur frequently on multiple scales on the ETP. These processes form the fundamental basis of its unique geography and enable it to generate considerable impacts on regional precipitation microphysics.

2.2. Radar and gauge network

11 Doppler weather radars are currently deployed for severe weather warning and forecast operations in this region. The specific locations and basic system specifications of these 11 radars are listed in Table 1. The radar type is specified according to its operating frequency and different manufacturers. SA/SC in Table 1 both mean S-band, whereas CD means C-band. The radial resolutions of SC and CD radars are configured as 250 m with an azimuthal resolution of 1°. The SA radars are set with resolution of 1000 m by 0.98°. The radar volume scan modes are all configured as the standard volume coverage pattern with sweep elevations set at 0.5°, 1.5°, 2.4°, 3.5°, 4.9°, 5.6°, 6.5°, 7.9°, 9.5°, 14.5°, and 19.5°. Such precipitation mode is used for meteorological operations. It takes about six minutes to complete a volume scan, and the base-level (level II) data are archived as volume scan files. The maximum radar reflectivity radial ranges in Table 1 are determined by the configurations of pulse repetition frequency (PRF), where SC and CD radars use the same PRF while SA adopts different PRF at different scan elevations. The coverage map of each of these 11 radars and heights of the lowest radar reflectivity that can be used to derive QPE are depicted in Fig. 2a. The radar network topology in Fig. 2a also shows its potential capability to observe various weather phenomena passing through the ETP.

There are 3264 rain gauges over the ETP (see Fig. 2b), most of which are tipping-bucket gauges with one-minute temporal resolution for real-time measurement, enabling them to capture the evolution of fine-scale precipitation events. The gauge observations are uploaded and transferred to the meteorological bureau at the municipal, provincial and national levels in order and in near real-time. Such dense rain gauge network also ensures the capability of SCIT to capture and represent storm-scale or regional precipitation processes.

The RT and SCIT based radar QPE algorithms are described in section 2.3. Before they are evaluated on an hourly basis, the hourly rainfall observations from rain gauges are quality-controlled via the procedure shown in Fig. 3: (1) the data series with interrupted transfer reports are removed to ensure the subsequent processing; (2) with the reflectivity aloft two empirical Z–R relationships (i.e., $Z = 640R^{1.6}$ and $Z = 200R^{1.6}$) are applied to estimate the possible maximum (R_{max}) and minimum (R_{min}) rain gauge hourly measurements, respectively. Those lying outside of [$R_{min}-5$, $R_{max}+5$] are removed from the raw dataset; (3) if the gauge observation is less than 0.1 mm but corresponding radar estimation is greater than 5 mm, the gauge is assumed jammed likely due to tree leaves, insects, and/or evaporation. If the gauge observation is greater than 5 mm but corresponding radar estimation is less than 0.1 mm, the bucket is suspected to have provided a false reading, and these observations are not used; (4) The remaining data are further checked using the ratio of rainfall estimation (for a given gauge location) using the nearest five surrounding gauges based on inverse distance weighting method (Lloyd, 2005), and the measured rainfall by the gauge at the same location. The gauge data point is abandoned in the subsequent cross-validation if the ratio is higher than four.

2.3. RT and SCIT-based Z–R relationship fitting

Before the implementation of Z–R relationships, radar base-level volume data is first quality-controlled to eliminate ground clutter using the fuzzy logic approach described in

Berenguer et al. (2006). Then, the radar data at polar coordinates are mapped onto Cartesian grids with a horizontal resolution of 0.01°× 0.01° and vertical resolution of 100 m, using the nearest neighbor and vertical interpolation approaches (Zhang et al., 2016). Multi-radar three-dimensional mosaic reflectivity is then created based on the temporally matched single radar dataset on Cartesian grids. At the grid location where observations from multiple radars are available, the following equation is used compute reflectivity value at this grid point.

$$Z(k,l)=\frac{\sum_{\mathrm{i}=1}^{\mathrm{N}} w_{\mathrm{i}}(k,l) Z_{\mathrm{i}}(k,l)}{\sum_{\mathrm{i}=1}^{\mathrm{N}} w_{\mathrm{i}}(k,l)}, \tag{1}$$

$$w_{\mathrm{i}}(k,l)=e^{-r} \tag{2}$$

where Z(k,l) and $Z_i(k,l)$ respectively represent the composite and single radar reflectivity at grid pixel (k,l); $w_\mathrm{i}(k,l)$ is the weight determined by the radar radial range distance r.

If the PBB ratio exceeds 60% for one radar, data from this radar is removed to enhance the quality of the multi-radar mosaic dataset in the overlapping region, or it is directly used if only one valid radar grid is available in the target coordinate (k, l). The multi-radar hybrid mosaic reflectivity (*MHMR*) is then constructed by selecting the reflectivity closest to the surface (i.e., lowest altitude) from the multi-radar mosaic gird data from 1000 m above MSL (see also Fig.2a). Four examples of *MHMR* with their moving trends are illustrated in Figs. 4 and 5, which will be further investigated in Sections 3.1 and 3.3.

Fig. 6 shows a diagram of the RT and SCIT-based QPE approaches. The *Z-R* relationship fittings in both approaches use grouped radar-gauge observation pairs $\{MHMR_i, G_i\}$. The radar based hourly QPE field are then calculated using the derived RT and SCIT-based *Z-R* relations. Since parameter b in $Z = AR^b$ is not sensitive to the precipitation type or state (Steiner and Smith, 2000), b is set to a constant (i.e., 1.6) when fitting the optimal parameter A by minimizing Eq. (3)

every six minutes:

$$\delta = \min \sum_{i=1}^{n} \left\{ (G_i - R_i)^2 + | G_i - R_i | \right\}, \tag{3}$$

where G_i is rainfall observation from gauge every six minutes; R_i is radar-based six-minutes rainfall derived using two time-adjacent radar rainfall rates estimated from $MHMR_i$.

Eq. (3) is a quadratic function and each RT or SCIT partitioned reflectivity group has its own fitted *Z-R* relation with independent coefficient *A* based on the radar-gauge pairs. The first term in Eq. (3) includes G^2, R^2, and $G*R$, which are quadratic terms and it will increase quickly if G_i and R_i are larger than 1 mm. The first-order term factors are added as the second term and it dominates Eq. (3) when G_i and R_i are less than 1 mm. Otherwise, the quadratic terms will dominate Eq. (3). The absolute bracket is necessary to avoid possible cancellation of positive and negative values.

Although similar steps are used to fit *Z–R* relationships, RT and SCIT methods differ in their grouping steps of $\{MHMR_i, G_i\}$ pairs. As in Fig. 6, RT method directly separates the $\{MHMR_i, G_i\}$ pairs into different groups according to $MHMR_i$ values from [20, 50] in 5 dBZ intervals. While SCIT method first separates the geographically distributed storm cells with an initial threshold of 20 dBZ and then further partitions them into regional groups by gradually increasing the step in 5 dBZ intervals. If the fitting process fails in the RT or SCIT partitioned reflectivity groups, the default Z=200$R^{1.6}$ is used, which is also used for the weak radar echoes less than 20 dBZ. Two independent radar hourly rainfall accumulations are derived using the *Z-R* relationships based on the RT and SCIT methods every six minutes, then they are evaluated using the precipitation events and evaluation metrics presented in Sections 3 and 4.

3. Precipitation events and microphysical characters

3.1. Precipitation Events

Based on the features of radar echoes and their moving directions retrieved by the Tracking Radar Echoes by Correlation method (TREC: Tuttle and Foote, 1990), four precipitation events (listed in Table 2) are selected to evaluate the hourly QPE products derived from radar using the RT- and SCIT-based approaches and examine the representative capabilities of RT and SCIT regarding the local precipitation features. Although these four events are all characterized by regional convective precipitation over complex terrain, they are selected independently to ensure the confidence in their performance assessment results. In the following, different features of these four precipitation events are briefly described.

The southwest vortex is a typical weather system with a helical rotation structure and is always accompanied by sufficient vapor from the Bay of Bengal influencing southwest China. Event 1 is a typical southwest vortex event that was captured by the Yibin, Yongchuan, Chongqing, and Qianjiang radar sites. Sample radar reflectivity echoes and corresponding TREC vector field at 0200UTC, 28 March 2014 are illustrated in Fig. 4a and Fig. 5a. Several storm cells were triggered in its frontal direction simultaneously. The maximum hourly rainfall amount observed by the gauge network reached about 29.3 mm at this time frame.

Large-scale stratiform or convection-stratiform mixed precipitation is the most frequent precipitation type over the ETP. Event 2 is a typical example of such event. Sample radar reflectivity echoes and corresponding TREC vector field at 1900UTC, 18 May 2014 are provided in Fig. 4b and Fig. 5b, which show that the radar echo initiated at the Hengduan Mountains moved from northwest to southeast, while the radar echoes initiated in the southwest moved along the southeast mountains at the same time. Several storm cells originated near the southeast mountains, and the maximum hourly rainfall amount measured by the gauge network was about 24.8 mm at this time frame.

During the summer monsoon season, precipitation induced by orographic enhancement over the windward slopes of mountains is the most common phenomena over the ETP. Events 3 and 4 both belong to this precipitation type. Example radar reflectivity echoes and TREC fields for event 3 are shown in Figs. 4c and 5c, which were moving toward Dalou Mountains accompanied by strong convective storm cells. Similarly, Figs. 4d and 5d illustrate sample reflectivity observations and corresponding TREC vector field for a time frame during event 4. During this event, the radar echoes and TREC fields were moving along the Hengduan Mountains and a parallel strong convective rain-band occurred and produced several deep convective storm cells. The maximum hourly rainfall amount recorded by the gauge network reached 82.9 mm during event 3 and 78.1 mm during event 4.

The intrinsic precipitation microphysical features associated with these four events are very important for verification and comparison of the RT- and SCIT-based algorithms and their representative capabilities of the precipitation spatial differences. Therefore, the radar-based storm-scale VPR analysis is conducted to further understand the precipitation features during these four events.

3.2. Storm-scale VPR

VPR is an important indicator of the microphysical features of precipitation. Using the identified storm cells on the MHMR field by SCIT, storm-scale VPR can be easily constructed and tracked using the multi-radar three-dimensional mosaic dataset. The VPR can also serve as a good indicator of the spatial differences and temporal evolution of precipitation. In this paper, the VPR is constructed based on the SCIT algorithm:

$$\overline{Z}_k = \frac{1}{N(S)} \sum_{(i,j)\in S} Z\left(i,j,k\right) \tag{4}$$

where $Z(i,j,k)$ is the reflectivity at (i, j) at the k_{th} level of the multi-radar three-dimensional mosaic grid; S is a restricted domain at the bottom of the storm identified by SCIT with a particular threshold (above 35 dBZ in this study) in the MHMR field; $\overline{Z}$ is the averaged reflectivity within the domain S at the k_{th} level with all reflectivity higher than 35 dBZ and $N(S)$ is the total number of grids within S. For a storm cell, reflectivity in the storm core is generally stronger than that outside the storm core. In addition, the storm-scale VPR is based on the storm cell bottom with a threshold of 35 dBZ as the identification parameter of SCIT. Therefore, all the radar echoes within the corresponding vertical column can be averaged and used on this column for further analysis.

3.3. Storm-scale VPR spatial differences and evolution

The instantaneous storm-scale VPR retrieved based on the method described in section 3.2 can be used to reveal the microphysical differences between storm cells. The VPRs were derived at different storm life time, depending on if its bottom can be successfully identified from the MHMR by SCIT. For an identified storm cell, its states at different time frames can be matched with each other. Based on the storm cell observations at different time frames, the VPR cluster can be derived spontaneously in its lifespan or at predefined time windows. In this paper, VPRs are obtained for four individual 1-h time frames during four different precipitation events. The retrieved VPR clusters are then used to investigate the precipitation characteristics and evolutions since they essentially represent the storm state at different time frames. The VPR numbers in a 1-h timespan are very limited, which further signifies the importance of investigating the VPR shape transformation and density (i.e., dense or sparse degree between individual VPRs). In this study, 14 storm cells on *MHMR* with the surface areas greater than 100 km^2 in a 1-h time window for the four events (see Fig. 4) are identified and selected to examine their intrinsic features. Details about these 14 storm cells, including starting and ending time and locations, are listed in Table 3. The consecutive storm-scale VPR profiles grouped as VPR clusters, as well as their main developing trends (moving directions) are shown in Fig. 7. The spatial differences and short-term evolution trends of these storm cells can be inferred by the profile shape and density of the VPR clusters.

3.3.1 Event 1

The prominence of the cell 1 VPR cluster below 2.5 km in Fig. 7a indicates the dominance of raindrop collision, which is a typical characteristic of convective precipitation. The convection of cell 1 is shallow, which is further demonstrated by Fig. 8a. Its evolution cannot be seen directly from the VPR cluster. However, the VPR profile density is relatively denser above 2.5 km, which implies that cell 1 was in a stable state above this height. The larger interval between the VPR profiles indicates that the convection was in an unstable developing stage below 2.5 km. The VPR cluster of cell 2 underwent large changes and evolved quickly into a weaker state in Fig.7b, while its peak reflectivity was located at the bottom and the VPR cluster was relatively denser below 4 km, indicating the convection was in a moderately stable state. Cells 3 (Fig. 7c) and 4 (Figs. 7d and 7e) are precipitation with ample moisture at the bottom (PAMB). The reflectivity profiles present a monotonically increasing trend toward the surface, which may be resulted from higher vapor density or larger raindrops at the bottom of these two storm cells. It can also be seen from the cross-section in Fig. 8(a) that reflectivity in cell 4 is much higher than that in cell 3 in the whole column, which implies heavier rainfall rates associated with cell 4. Both cell 3 and 4 are in a stable state above 4 km. However, cell 3 had undergone a short-term transition which persisted just for four time frames, whereas cell 4 was in the most complicated transition process among all the 14 storm cells. In particular, the VPR profile in cell 4 was gradually enhanced as the reflectivity became stronger below 4 km and finally reached its peak state in Fig. 7d. The VPR profile then transformed into a gradually weakening state in Fig. 7e, accompanying the weaker and weaker reflectivity below 4km. In addition, the sparser VPR cluster below 4 km indicates that it was in a more unstable state than the other three cells in this storm event.

3.3.2 Event 2

The differences of near-surface reflectivity in cells 5-8 can be directly seen from Fig. 8c-e, which are all in gradually weakening stages. Their VPR clusters are denser in layers below 1.5 km and the shallow convection may dominate during their lifespan period. The maximum reflectivity of cell 5 appears below 1.5 km with a vertical inflection point in Figs. 7f. It seems that cell 5 belongs to a mixed phase precipitation composited by stratiform and shallow convection. The hydrometeors above 4 km form another peak reflectivity for cell 5, and it was accompanied by a storm core embedded in its column (see Fig. 8c), which is intrinsically different from the bottom. Cell 6 is another example of PAMB, and its reflectivity increased monotonically and abruptly around 2 km toward the surface with its maximum reflectivity located near the bottom (see Figs. 7g and 8d). This phenomenon persisted during the whole analysis period.

Cells 7 and 8 in Figs. 7h-i are similar to each other at all levels. They occurred on the same bottom of the precipitation cloud, but were partitioned by SCIT due to the reflectivity gap between them. The VPR inflection points emerged near 1.5-1.8 km height with peak reflectivity at 4 km height, which is resulted from the melting layer enhancement. Another reflectivity peak was located below 2 km that accounts for the PAMB or shallow convection near the surface. This phenomenon can be seen in Fig. 8e with a precipitation cloud core floating between 2.5-5.5 km, where the maximum radar reflectivity had exceeded 40 dBZ.

3.3.3 Event 3

Cells 9 and 10 are examples of strong convective precipitation with their cloud top exceeding 12 km. The VPR cluster of cell 9 in Fig. 7j shows relatively abrupt fluctuations. Its strong convective cell structure can be clearly seen from the cross-section in Fig. 8f at 2-5 km with its maximum reflectivity exceeding 50 dBZ, while it was in a gradually weakened stage. Radar miscalibration severely affected the VPR of cell 10 in Fig. 7k, and the reflectivity discontinuities were observed between 3 km and 4 km in the cross-section shown in Fig. 8g. Nevertheless, its VPR density demonstrated that it was in a stable state above 2 km.

3.3.4 Event 4

The VPR clusters of cells 11–14 in Figs. 7l-o are similar to each other above 4 km and no obvious transition boundaries exist between adjacent VPR profiles. This indicates that the upper layers above 4 km are in stable and quasi-stationary states. However, heterogeneous characteristics can be seen below 4 km.

Cell 11 was featured with PAMB below 2 km but with stratiform cloud characteristics above deduced from its VPR shapes. Its reflectivity increased monotonically below 2 km toward the surface and the reflectivity about 35 dBZ dominates its bottom with an inflection point located at 2 km (see Fig.7l). The relatively high reflectivity near 4 km height was resulted from melting layer enhancement, which is further illustrated by Fig. 8h. Cell 12 also presents severe convection below 2 km and is similar to cell 14 at the bottom (see Figs. 8i and 8k). However, its bottom averaged reflectivity is a little higher than that of cell 14 (see Figs. 5m and 5o).

Cells 13 and 14 both have a vertically uniform transition layer between 1.5 km and 4 km (Figs. 7n-o). Their cross-sections present maximum reflectivity over 50 dBZ in Figs. 8j-k. There are more reflectivity grids exceeding 40 dBZ at the bottom in Fig. 8k than in Fig. 8j, which means that cell 14 may have heavier rainfall rates than cell 13.

The spatial and temporal evolution of these storm-scale VPR clusters demonstrates that each storm cell has heterogeneous microphysics and precipitation characters. When their bottom reflectivity is transformed into radar rainfall rate, optimal instantaneous *Z–R* relationships are crucial to enhance radar QPE performance. It is worth noting again that the RT and SCIT methods treat the similar radar echoes in a different way, which produces different representative capabilities and radar QPE scores.

4. Evaluation results and discussion

4.1. Evaluation Metrics

The gauge stations over the ETP are uniformly separated into two independent groups: the training dataset containing 1631 stations and the test dataset containing 1633 stations (see Fig. 2b). Only the training dataset is used for the derivation of *Z–R* relationships. The test dataset is used for verification of the radar-derived rainfall products. The evaluation metrics, including the bias ratio (E_{BR}), mean absolute error (E_{MA}), root-mean-square error (E_{RMS}), and Pearson correlation coefficient (E_{CC}), are respectively defined as follows:

$$E_{BR} = \frac{\bar{r}}{\bar{g}}, \tag{5a}$$

$$E_{MA} = \frac{1}{n}\sum_{i=1}^{n}\left|r_i - g_i\right|, \tag{5b}$$

$$E_{RMS} = \sqrt{\frac{1}{n}\sum_{i=1}^{n}\left|r_i - g_i\right|^2}, \tag{5c}$$

$$E_{CC} = \frac{\sum_{i=1}^{n}(r_i - \bar{r})(g_i - \bar{g})}{\sqrt{\sum_{i=1}^{n}(r_i - \bar{r})^2}\sqrt{\sum_{i=1}^{n}(g_i - \bar{g})^2}}, \tag{5d}$$

where g and r are hourly rainfall measurements from gauge and radar, respectively; $\bar{g}$ and $\bar{r}$ represent the sample averages of hourly rainfall measurements within the target region from gauge and radar, respectively.

$$\bar{g} = \frac{1}{n}\sum_{i=1}^{n} g_i \tag{6a}$$

$$\bar{r} = \frac{1}{n}\sum_{i=1}^{n} r_i \tag{6b}$$

E_{BR} is related to the radar QPE regional areal error, which refers to the comparison of averaged-rainfall from radar and gauges over the study domain. Generally, the more E_{BR} concentrates at [0.8, 1.2], the better consistency between radar rainfall estimation and gauge observation can be achieved. Otherwise, if more E_{BR} scores lie in $(1.2,+\infty)$ or $[0, 0.8)$, overestimation or underestimation of radar QPE will be concluded, respectively. E_{MA} and E_{RMS} are important indicators of the radar QPE local error, which are basically computed through pixel-by-pixel radar-gauge comparison. Smaller E_{MA} and E_{RMS} imply better algorithm performances. $E_{MA}(\text{SCIT})<E_{MA}(\text{RT})$ and $E_{RMS}(\text{SCIT})<E_{RMS}(\text{RT})$ indicate that the SCIT-based approach has better performance than the RT-based algorithm. E_{CC} reflects the correlation between the radar rainfall estimation and gauge observations. Larger E_{CC} also indicates better algorithm performance. The probability of $E_{CC}(\text{SCIT})<E_{CC}(\text{RT})$ represents the radar QPE improvement of the SCIT-based algorithm with respect to the RT-based algorithm.

The performance of RT- and SCIT-based methods can be easily deduced from these four independent scores and the score comparison statistics for all events. Ideally, the improved radar QPE should have low regional error (i.e., E_{BR} should be close to 1) and low local error (i.e., smaller values of E_{MA} and E_{RMS}, and larger E_{CC}). In addition, large errors may be averaged if too many small or zero observations exist in the test dataset. Therefore, the scores in Eq. (5) are calculated only when the gauge hourly rainfall observation is greater than 0.1 mm, and the number of gauges in the test dataset should exceed 10 to ensure confidence in the evaluation results. These scores are calculated first at the same temporal resolution as the radar hourly QPE (i.e., every six minutes) to obtain direct evaluation scores for two radar QPE fields. These scores are then compared one by one, and statistics are made according to the predefined score comparison criteria.

4.2. Results

The results of E_{BR}, E_{MA}, E_{RMS}, and E_{CC} for the four events are listed in Table 4. According to the statistics in Table 4, SCIT presents better than RT by 2.03% for event 1, 13.27% for event 2, 39.8% for event 3, and 43.49% for event 4 in terms of $E_{BR} \in [0.8,1.2]$. The SCIT-based approach is better than RT-based algorithm by 8.56% for event 1, 16.71% for event 2, 40.62% for event 3, and 45.73% for event 4 in terms of $E_{BR} > 1.2$, but marginally worse than the RT-based approach by 6.53% for event 1, 3.43% for event 2, 0.82% for event 3, and 2.24% for event 4 according to $E_{BR} < 0.8$. E_{BR} of RT are more aggregated in $(1.2,+\infty)$ but less aggregated in [0.8, 1.2]. In other words, for all four events, the SCIT-based approach has much better performance than the RT-based method in regions where overestimation may occur, whereas in the regions where underestimation is evident they show similar performance. Also, it should be noted that the pointwise radar and gauge differences are neglected in the calculation of E_{BR}. As such, E_{BR} can be considered a metric representing the mean-field-bias of radar QPE, but not the local bias.

SCIT indicates a clear superiority over RT according to the probability of $E_{\mathrm{MA}}(\mathrm{SCIT}) < E_{\mathrm{MA}}(\mathrm{RT})$, $E_{\mathrm{RMS}}(\mathrm{SCIT}) < E_{\mathrm{RMS}}(\mathrm{RT})$ and $E_{\mathrm{CC}}(\mathrm{SCIT}) > E_{\mathrm{CC}}(\mathrm{RT})$ for all events. The lowest probabilities of $E_{\mathrm{MA}}(\mathrm{SCIT}) < E_{\mathrm{MA}}(\mathrm{RT})$ and $E_{\mathrm{RMS}}(\mathrm{SCIT}) < E_{\mathrm{RMS}}(\mathrm{RT})$ are 89.04% and 81.76%, respectively (i.e., for event 4), which are still very high. $E_{\mathrm{CC}}(\mathrm{SCIT}) > E_{\mathrm{CC}}(\mathrm{RT})$ also has similar statistics to E_{MA} and E_{RMS} in all events with the highest probability 91.63% for event 3 and the lowest probability of 75.74% for event 4.

All the quantitative evaluation results indicate that the radar QPE local error has been improved by SCIT and its scores of E_{MA}, E_{RMS}, E_{CC} are all better than those of RT at most time frames for all the evaluation events. In order to further demonstrate the superior performance of the SCIT-based rainfall algorithm, Fig. 9 illustrates the scatter plots of radar derived hourly rainfall using RT and SCIT approaches versus gauge hourly rainfall observations for all four events combined. Fig. 9 shows that although radar rainfall products derived using both RT and SCIT-based approaches agree well with rain gauge observation, the SCIT-based approach has much better performance. Since the same $\{MHMR_i, G_i\}$ pairs are used in the fitting process to minimize Eq. (1) by both methods. The evaluation score differences and improvements can be attributed to the partition of radar echoes using the SCIT algorithm, and the coexistence of multiple precipitation processes are represented better by the SCIT algorithm.

4.3. Representative capability of RT and SCIT method

The statistical comparison results in section 4.2 are essentially related to the representative capability of *Z–R* relationship distribution in the two methods. The radar QPE local error improvement can be attributed to the utilization of SCIT to partition MHMR into different regions, so that local precipitation features within the independent storm cells or regimes can be captured and refined with more representative *Z–R* relationships based on the radar-gauge feedback mechanism. Example spatial distributions of *Z–R* relationships at four time frames during the four precipitation events are illustrated in Fig. 10. Figs. 10(a)(c)(e)(g) are for the RT-based approach. RT treats the similar radar echoes as homogenous no matter they are within the same or different storm cells. The *A*-coefficients are assigned only according to the reflectivity intervals. However, the homogeneous *A*-coefficients cannot represent the storm-scale or regional differences according to the VPR analysis in section 3.3. The radar QPE overestimation of RT in one local region may be comprised by its underestimation in another local region. As a result, the radar QPE local error cannot be mitigated effectively.

The most important difference between the RT- and SCIT-based methods is that the SCIT separates MHMR into different geographical regions. As depicted in Figs. 10(b)(d)(f)(h), the radar echo partitions capture and refine the storm-scale and regional precipitation differences. More *A*-coefficients than RT are used to retrieve radar rainfall rates to incorporate these differences. It is an important improvement to the radar QPE local error, with better E_{MA}, E_{RMS}, and E_{CC} results. Therefore, the spatial distribution of the *Z-R* relationships of SCIT is more representative than RT to capture the multiple precipitation microphysical differences.

5. Summary and Future Work

Two radar QPE algorithms (i.e., SCIT and RT methods) based on the radar-gauge feedback mechanism are developed and evaluated using radar and gauge observations over the ETP. The analysis and comparison results have shown that:

(1) The storm-scale VPR, based on multi-radar reflectivity mosaic and SCIT identification results, is used to investigate the precipitation microphysics of four typical weather events in 2014. These precipitation events are all important scenarios with regional precipitation characteristics. The VPR clusters show that although the storm cells with similar radar echoes on the *MHMR*, they were actually featured by heterogeneous storms with different precipitation microphysical processes.

(2) The SCIT-based rainfall algorithm performs better than the RT-based approach for most time frames during these four events. The superiority of SCIT over RT can be attributed to its better capability to capture the regional precipitation characteristics. The effective partition of radar echoes is an important step to make SCIT be able to identify local differences and group radar-gauge pairs accordingly. It has been concluded that SCIT is a useful tool to resolve radar QPE local errors associated to the non-uniform spatial distribution of rainfall.

(3) Compared to the RT-based method, the distribution of *Z-R* relations in SCIT method is featured with more various *Z-R* parameters, which represent the regional precipitation characteristics. This, again, demonstrates the superiority of the SCIT method in capturing the local precipitation variabilities.

Although the superior performance of SCIT method to RT are referenced above, more efforts should be carried out to enhance the performances of radar QPE for Tibetan Plateau (TP). In particular, the following items will be investigated in future to address the QPE challenges over complex terrain in TP.

(1) The rainfall methodologies based on polarimetric radar variables (e.g., Chen et al. 2017) should be implemented in future after the dual-polarization upgrade. The dual-polarization upgrade is also expected to provide a promising tool to recover the partially blocked radar echoes, and subsequently improve the QPE performance based on weaker radar echoes introduced by PBB.

(2) More effective BB identification and correction methods are also very valuable to reduce the overestimation of radar QPE. Low radar beams of the Doppler weather radars over TP are generally blocked by the complex terrain, while the high-elevation scans greatly suffer from BB contamination. The VPR identification and enhancement method (e.g., VPR-IE in Wen et al. 2013) can help to mitigate BB effects and this will be an important future work.

(3) The regional precipitation characteristics over TP should be highlighted and carefully treated, especially the precipitation climatology, terrain and environmental effects which are all noticeable and regionally featured. The statistical distribution of *Z-R* relationships derived based on long-term radar and surface rainfall observations should be investigated more to improve radar QPE for regional hydrometeorological applications.

Acknowledgements: This research was primarily supported by the National Natural Science Foundation of China (NSFC) under Grants 91437214, 41705018, and 41601065. Additionally, Y. Gou was partially supported by Zhejiang Provincial Natural Science Fund through award LY17D050005. Y. Ma was partially supported by the Open Fund from the Key Laboratory for Aerosol-Cloud-Precipitation of China Meteorological Administration (No. KDW1605). The rain gauge data were provided by China Meteorological Administration.

References

Alfieri, L., P. Claps, and F. Laio, 2010: Time-dependent Z-R relationships for estimating rainfall fields from radar measurements, Nat. Hazards Earth Syst. Sci., 10, 149-158.

Berenguer, M., D. Sempere-Torres, C. Corral, and R. Sánchez-Diezma, 2006: A Fuzzy Logic Technique for Identifying Nonprecipitating Echoes in Radar Scans. J. Atmos. Oceanic Technol., 23, 1157-1180.

Bringi, V. N., and V. Chandrasekar, 2001: Polarimetric Doppler Weather Radar: Principles and Applications. Cambridge University Press, 664 pp.

Chandrasekar, V., H. Chen, and B. Philips, 2018: Principles of high-resolution radar network for hazard mitigation and disaster management in an urban environment. J. Meteor. Soc. Japan, 96A, https://doi.org/10.2151/jmsj.2018-015.

Chapon, B., G. Delrieu, M. Gosset, and B. Boudevillain, 2008: Variability of rain drop size distribution and its effect on the Z-R relationship: A case study for intense Mediterranean rainfall. Atmos. Res., 87, 52-65.

Chen, H., and V. Chandrasekar, 2015: The quantitative precipitation estimation system for Dallas-Fort Worth (DFW) urban remote sensing network. Journal of Hydrology, 531, 259-271.

Chen, H., V. Chandrasekar, and R. Bechini, 2017: An Improved Dual-Polarization Radar Rainfall Algorithm (DROPS2.0): Application in NASA IFloodS Field Campaign. J. Hydrometeor., 18, 917-937.

Cifelli, R., and V. Chandrasekar, 2010: Dual-polarization radar rainfall estimation. Rainfall: State of the Science, Geophys. Monogr., vol. 191, Amer. Geophys. Union, 105-126.

Cifelli, R., V. Chandrasekar, H. Chen, and L. E. Johnson, 2018: High resolution radar quantitative precipitation estimation in the San Francisco Bay Area: Rainfall monitoring for the urban environment. J. Meteor. Soc. Japan, 96A, https://doi.org/10.2151/jmsj.2018-016.

Crochet, P., 2009: Enhancing radar estimates of precipitation over complex terrain using information derived from an orographic precipitation model. Journal of Hydrology, 377, 417-433.

Fulton, R. A., J. P. Breidenbach, D.-J. Seo, and D. A. Miller, 1998: The WSR-88D rainfall algorithm. Wea. Forecasting, 13, 377-395.

Gou, Y., L. Liu, J. Yang, C. Wu, 2014: Operational application and evaluation of the quantitative precipitation estimates algorithm based on the multi-radar mosaic. Acta Meteor Sinica, 72(4), 731-748. doi:10.11676/qxxb2014.050.(in Chinese)

Gou, Y. B., L. Liu, D. Wang, L. Zhong, and C. Chen, 2015: Evaluation and analysis of the Z-R storm-grouping relationships fitting scheme based on storm identification. Torrential Rain and Disasters. 34(01), 1-8. doi: 10.3969/j.issn.1004-9045.2015.01.001. (in Chinese)

James V. Rudolph and Friedrich, K., 2013: Seasonality of Vertical Structure in Radar-Observed Precipitation over Southern Switzerland. J. Hydrometeor., 14, 318-330.

Johnson, J., P. L. MacKeen, A. Witt, E. D. W. Mitchell, G. J. Stumpf, M. D. Eilts, and K. W. Thomas, 1998: The storm cell identification and tracking algorithm: An enhanced WSR-88D algorithm. Wea. Forecasting, 13, 263-276.

Kitchen, M., R. Brown, and A. G. Davies, 1994: Real-time correction of weather radar data for the effects of bright band, range and orographic growth in widespread precipitation. Quart. J. Roy. Meteor. Soc., 120, 1231-1254.

Lee, G. W., and I. Zawadzki, 2005: Variability of Drop Size Distributions: Time-scale dependence of the variability and its effects on rain estimation. J. Appl. Meteor., 44, 241-255.

Lloyd, C. D., 2005: Assessing the effect of integrating elevation data into the estimation of monthly precipitation in Great Britain. Journal of Hydrology, 308(1), 128-150.

Nesbitt, S. W., R. Cifelli, and S. A. Rutledge, 2006: Storm Morphology and Rainfall Characteristics of TRMM Precipitation Features. Mon. Wea. Rev., 134, 2702-2721, doi: 10.1175/MWR3200.1

Rosenfeld, D., D.B. Wolff, and E. Amitai, 1994: The Window Probability Matching Method for Rainfall Measurements with Radar. J. Appl. Meteor., 33, 682-693.

Seo, D-J., J. P. Breidenbach, and E. R. Johnson, 1999: Real-time estimation of mean field bias in radar rainfall data. J. Hydrol., 223, 131-147.

Shimamura, S., V. Chandrasekar, T. Ushio, and et al., 2016: Probabilistic Attenuation Correction in a Networked Radar Environment. IEEE Transactions on Geoscience and Remote Sensing. 54(12), 6930-6939.

Smith, J. A., E. Hui, M. Steiner, M. L. Baeck, W. F. Krajewski, and A. A. Ntelekos,2009, Variability of rainfall rate and raindrop size distributions in heavy rain, Water Resour. Res., 45, W04430, doi:10.1029/2008WR006840.

Steiner, M. and J.A. Smith, 2000: Reflectivity, Rain Rate, and Kinetic Energy Flux Relationships Based on Raindrop Spectra. J. Appl. Meteor., 39, 1923-1940.

Tuttle, J. and G. Foote, 1990: Determination of the Boundary Layer Airflow from a Single Doppler Radar. J. Atmos. Oceanic Technol., 7, 218-232.

Wen, Y., Q. Cao, P.-E. Kirstetter, and et al., 2013: Incorporating NASA spaceborne radar data into NOAA National Mosaic QPE system for improved precipitation measurement: A physically based VPR identification and enhancement method. J. Hydrometeor., 14, 1293-1307.

White, A. B., P. J. Neiman, F. M. Ralph, D. E. Kingsmill, and P. O. G. Persson, 2003: Coastal Orographic Rainfall Processes Observed by Radar during the California Land-Falling Jets Experiment. J. Hydrometeorol., 4, 264-282.

Willie, D., et al., 2016: Regional polarimetric quantitative precipitation estimation over South Carolina. Proc. of 2016 IEEE International Geoscience and Remote Sensing Symposium (IGARSS), Beijing, doi: 10.1109/IGARSS.2016.7729557.

Willie, D., et al., 2017: Evaluation of Multisensor Quantitative Precipitation Estimation in Russian River Basin. Journal of Hydrologic Engineering, 22(5), E5016002, doi: 10.1061/(ASCE)HE.1943-5584.0001422.

Yoshikawa, E., T. Ushio, Z. Kawasaki, and V. Chandrasekar, 2012: Dual-directional radar observation for preliminary assessment of the Ku-band broadband radar network. J. Atmos. Oceanic Technol., 29, 1757-1768.

Yoshikawa, E., V. Chandrasekar, and T. Ushio, 2014: Raindrop size distribution (DSD) retrieval for X-band dual-polarization radar. J. Atmos. Oceanic Technol., 31, 387-403.

Zhang, J., K. Howard, C. Langston, and et al., 2016: Multi-Radar Multi-Sensor (MRMS) Quantitative Precipitation Estimation: Initial Operating Capabilities. Bull. Amer. Meteor. Soc., 97, 621-638.

Table Captions:

Table 1. Configuration of the Doppler radar network over the eastern Tibetan Plateau (ETP).

Table 2. Typical weather events over the ETP in 2014.

Table 3. Time and locations of the storm cell scale VPR clusters shown in Fig. 7. It should be noted that since cells 1, 3, and 4 are adjacent, a long cross-section line is selected to cover all the three storm cells. Similar idea is applied for storm cells 7 and 8 (see also Figs. 4 and 8).

Table 4. Evaluation results of the RT- and SCIT-based radar rainfall approaches for four different precipitation events.

Table 5. Evaluation results of the RT- and SCIT-based radar rainfall approaches at four individual time frames during four different events.

Table 1. Configuration of the Doppler radar network over the eastern Tibetan Plateau (ETP).

Radar name	Radar type	Max range (km)	Radial Resolution (m)
Chengdu	SC	140	250
Mianyang	CD	125	250
Nanchong	SC	150	250
Dazhou	SC	150	250
Yibin	SC	150	250
Leshan	SC	150	250
Guangyuan	SC	150	250
Yongchuan	SA	230	1000
Wanzhou	SA	230	1000
Chongqing	SA	230	1000
Qianjiang	CD	165	250

Table 2. Typical weather events over the ETP in 2014

Weather Event	Radar echo moving direction	Time Span	Number of time frames	Affected parts in the target region
Event 1	Southwest vortex	1400 UTC 27 Mar 2014 to 0900 UTC 30 Mar 2014	445	South and east
Event 2	West to east	1100 UTC 18 May 2014 to 0600 UTC 21 May 2014	476	Center and south
Event 3	Southeast to northwest	0730 UTC 2 Jun 2014 to 0800 UTC 5 Jun 2014	491	Center, east and north
Event 4	South to north	0900 UTC 30 Jul 2014 to 0800 UTC 1 Aug 2014	471	West and south

Table 3. Time and locations of the storm cell scale VPR clusters shown in Fig. 7. It should be noted that since cells 1, 3, and 4 are adjacent, a long cross-section line is selected to cover all the three storm cells. Similar idea is applied for storm cells 7 and 8 (see also Figs. 4 and 8).

Cell No	Number of VPR Profiles	Time Period		Lat and Long of the Storm Cells' Cross Section Line	
		Start Time	End Time	Start (long, lat)	End (long, lat)
1	11	0130 UTC 28 Mar 2014	0230 UTC 28 Mar 2014	(105.25°,29.20°)	(106.42°,30.5°)
2	5	0136 UTC 28 Mar 2014	0154 UTC 28 Mar 2014	(108.9°, 29.75°)	(109.25°, 29°)
3	4	0148 UTC 28 Mar 2014	0206 UTC 28 Mar 2014	(105.25°,29.20°)	(106.42°, 30.5°)
4	8	0148 UTC 28 Mar 2014	0230 UTC 28 Mar 2014	(105.25°,29.20°)	(106.42°, 30.5°)
5	4	1900 UTC 18 May 2014	1918 UTC 18 May 2014	(105.35°,29.35°)	(106°, 29.85°)
6	4	1900 UTC 18 May 2014	1918 UTC 18 May 2014	(108.15°, 30.9°)	(108.75°, 31.5°)
7	7	1900 UTC 18 May 2014	1936 UTC 18 May 2014	(105°, 29.4°)	(106.50°, 30.65°)
8	8	1900 UTC 18 May 2014	1942 UTC 18 May 2014	(105°, 29.4°)	(106.50°, 30.65°)
9	10	1106 UTC 02 Jun 2014	1200 UTC 02 Jun 2014	(106.55°,30.95°)	(107.25°, 30.7°)
10	11	1100 UTC 02 Jun 2014	1200 UTC 02 Jun 2014	(107.05°, 31.9°)	(107.7°, 31.9°)
11	6	0006 UTC 31 July 2014	0036 UTC 31 July 2014	(103.9°, 29.75°)	(104.25°, 31.15°)
12	10	0006 UTC 31 July 2014	0100 UTC 31 July 2014	(103°, 29.95°)	(104°, 30.65°)
13	10	0006 UTC 31 July 2014	0042 UTC 31 July 2014	(103°, 30.25°)	(104°, 30.85°)
14	7	0012 UTC 31 July 2014	0100 UTC 31 July 2014	(104.00°,31.40°)	(104.65°, 30.85°)

Table 4. Evaluation results of the RT- and SCIT-based radar rainfall approaches for four different precipitation events.

Weather Events	Sample Size	Score Statistics of E_{BR}, E_{MA}(mm), E_{RMS}(mm) and E_{CC}								
		RT			SCIT			E_{MA}(SCIT) < E_{MA}(RT)	E_{RMS}(SCIT) < E_{RMS}(RT)	E_{CC} (SCIT) > E_{CC} (RT)
		E_{BR} <0.8	$E_{BR} \in$ [0.8,1.2]	E_{BR} >1.2	E_{BR} <0.8	$E_{BR} \in$ [0.8,1.2]	E_{BR} >1.2			
Event 1	445	1.58	89.64	8.78	8.11	91.67	0.22	90.09	84.46	89.86
Event 2	476	4.81	75.06	20.14	8.24	88.33	3.43	89.93	82.38	82.38
Event 3	491	5.51	51.22	43.27	6.33	91.02	2.65	95.71	93.67	91.63
Event 4	471	1.26	32.43	66.31	3.50	75.92	20.58	89.04	81.76	75.74

Table 5. Evaluation results of the RT- and SCIT-based radar rainfall approaches at four individual time frames during four different events.

Weather Event	Time (UTC)	E_{BR}		E_{MA}(mm)		E_{RMS}(mm)		E_{CC}	
		RT	SCIT	RT	SCIT	RT	SCIT	RT	SCIT
Event 1	0230, 28 Mar 2014	0.97	0.81	1.56	1.04	2.23	1.74	0.59	0.78
Event 2	2000, 18 May 2014	1.08	0.87	1.05	0.70	1.47	1.12	0.46	0.75
Event 3	1200, 02 Jun 2014	1.71	1.05	4.51	1.93	7.10	3.71	0.92	0.95
Event 4	0100, 31 Jul 2014	1.33	0.95	2.70	1.24	4.22	2.33	0.82	0.92

Figure Captions:

Fig. 1. The digital elevation map (DEM) of (a) China and (b) the study region. The black rectangle in (a) indicates the location of study domain with respect to whole China.

Fig. 2. Doppler radar and rain gauge network over ETP: (a) the maximum radar coverage ranges (black circles) of each radar and heights of multi-radar hybrid mosaic reflectivity (MHMR); (b) distribution of rain gauges. The 1631 gauge stations in red are used for deriving radar rainfall algorithms, whereas the 1633 gauges in blue are used for validation of radar-derived rainfall products.

Fig. 3. Flowchart of the rain gauge data quality control process.

Fig.4. Storm cells identified by SCIT algorithm on the multi-radar hybrid mosaic reflectivity (MHMR) at (a) 0200 UTC, 28 Mar 2014; (b) 1900 UTC, 18 May 2014; (c)1130 UTC, 2 Jun 2014; and (d) 0100 UTC, 31 Jul 2014. The circles represent the main coverage of the identified storm cells and the lines indicate location of the cross-sections in Fig. 8.

Fig. 5. Digital elevations and radar echo moving directions retrieved by TREC at (a) 0200 UTC, 28 Mar 2014; (b) 1900 UTC, 18 May 2014; (c) 1130 UTC, 2 Jun 2014; and (d) 0100 UTC, 31 Jul 2014.

Fig. 6. Conceptual diagram of the RT and SCIT-based radar rainfall approaches.

Fig. 7. Storm-scale VPR clusters for the 14 storm cells illustrated in Fig. 4 in 1-h span. The arrows denote the moving directions of the VPRs. In particularly, cell 4 was gradually enhanced in (d) but weakened in (e). The number of VPR profiles for each storm cell is listed in Table 3.

Fig. 8. Vertical profiles of reflectivity for the 14 storm cells indicated in Fig. 4. (a) Cells 1, 3, and 4; (b) cell 2; (c) cell 5; (d) cell 6; (e) cells 7 and 8; (f) cell 9; (g) cell 10; (h) cell 11; (i) cell 12; (j) cell 13; and (k) cell 14. The starting and ending locations (Lat/Long) of each cross section line are marked on the x-axes, and the vertical columns of the storm cells are denoted by the dashed-lines. More information about these 14 storm cells can be found in Table 3.

Fig. 9. Scatter plots of radar-derived hourly rainfall versus gauge observations. (a) and (b) are averaged RT- and SCIT-based rainfall estimates across four events; (c) and (d) are RT- and SCIT-based rainfall estimates for four time frames at 0230 UTC 28 Mar 2014, 2000 UTC 18 May 2014, 1200 UTC 02 Jun 2014, and 0100 UTC 31 Jul 2014.

Fig. 10. Spatial distribution of the *Z–R* relationships [b = 1.6, the color represents value of coefficient A]. (a), (c), (e), and (g) are for the RT-based approach at 0200 UTC 28 Mar 2014, 1900 UTC 18 May 2014, 1130 UTC 2 Jun 2014, and 0100 UTC 31 Jul 2014, respectively. (b), (d), (f), and (h) are for the SCIT-based approach at the same time frames.

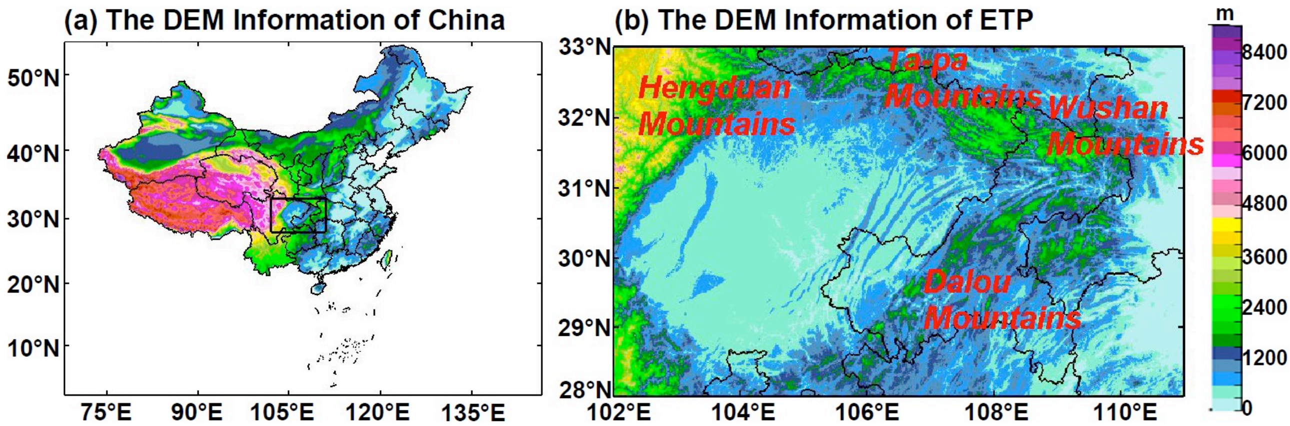

Fig. 1. The digital elevation map (DEM) of (a) China and (b) the study region. The black rectangle in (a) indicates the location of study domain with respect to the whole China.

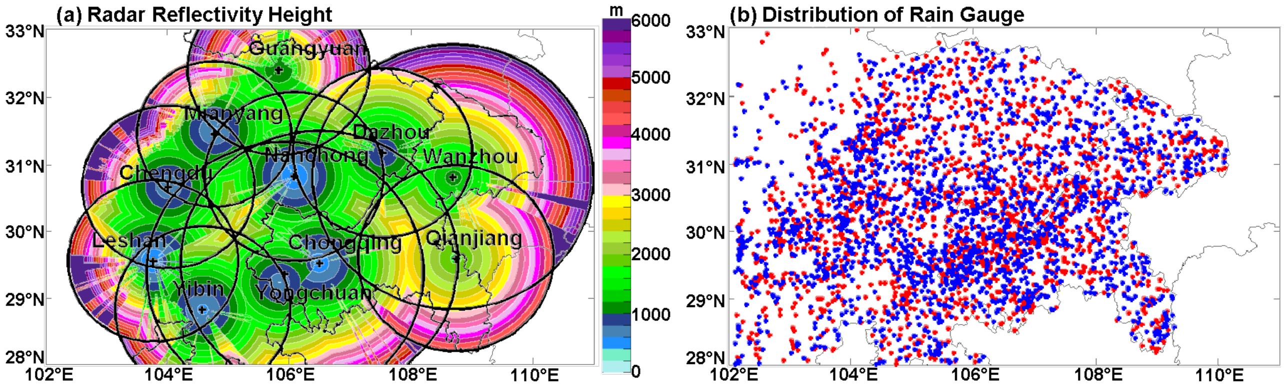

Fig. 2. Doppler radar and rain gauge network over ETP: (a) the maximum radar coverage ranges (black circles) of each radar and heights of multi-radar hybrid mosaic reflectivity (MHMR); (b) distribution of rain gauges. The 1631 gauge stations in red are used for deriving radar rainfall algorithms, whereas the 1633 gauges in blue are used for validation of radar-derived rainfall products.

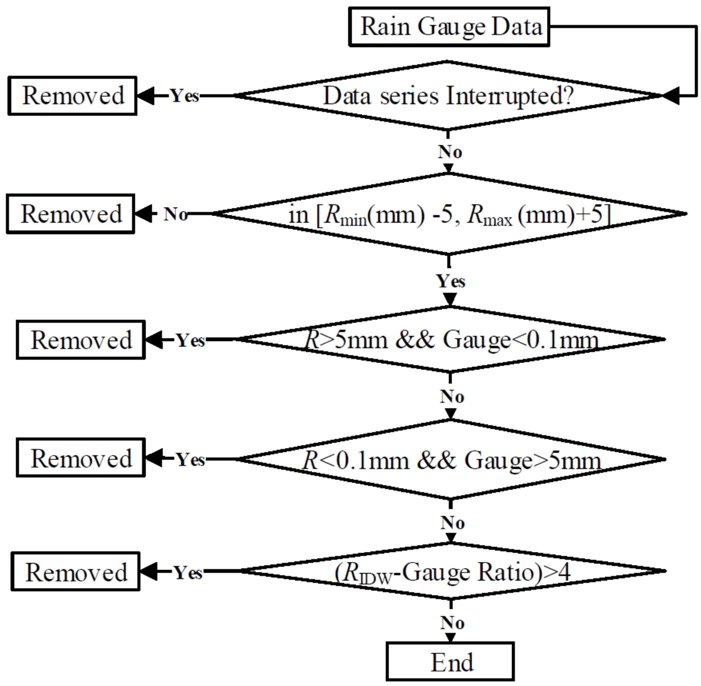

Fig. 3. Flowchart of the rain gauge data quality control process.

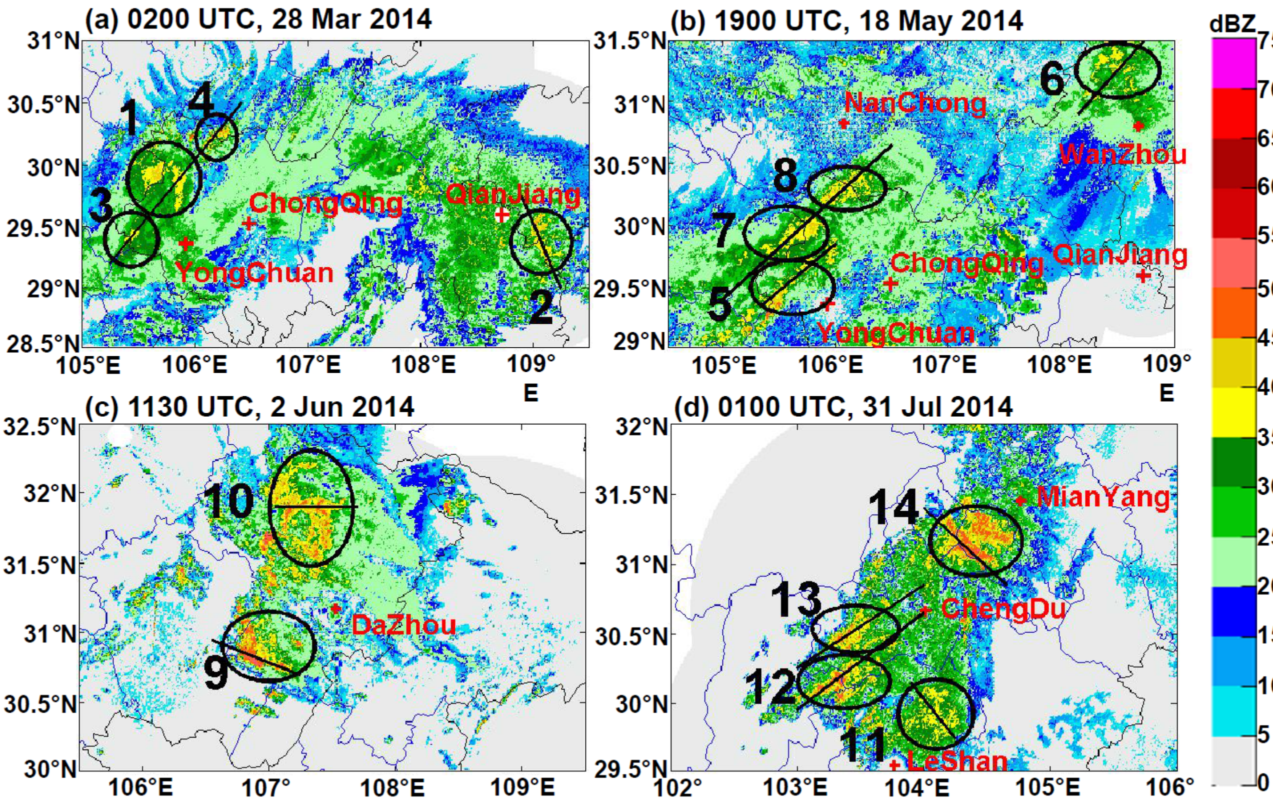

Fig. 4. Storm cells identified by SCIT algorithm on the multi-radar hybrid mosaic reflectivity (MHMR) at (a) 0200 UTC, 28 Mar 2014; (b) 1900 UTC, 18 May 2014; (c)1130 UTC, 2 Jun 2014; and (d) 0100 UTC, 31 Jul 2014. The circles represent the main coverage of the identified storm cells and the lines indicate location of the cross-sections in Fig. 8.

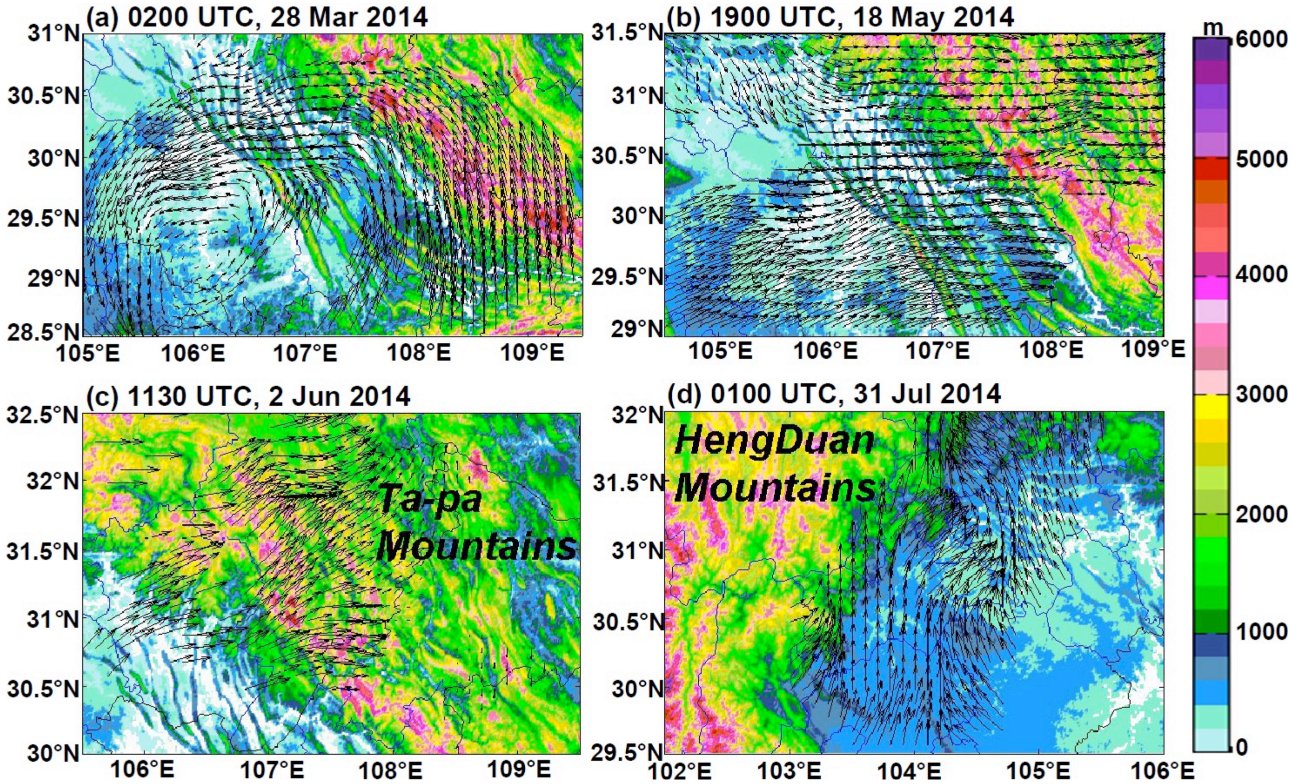

Fig. 5. Digital elevations and radar echo moving directions retrieved by TREC at (a) 0200 UTC, 28 Mar 2014; (b) 1900 UTC, 18 May 2014; (c) 1130 UTC, 2 Jun 2014; and (d) 0100 UTC, 31 Jul 2014.

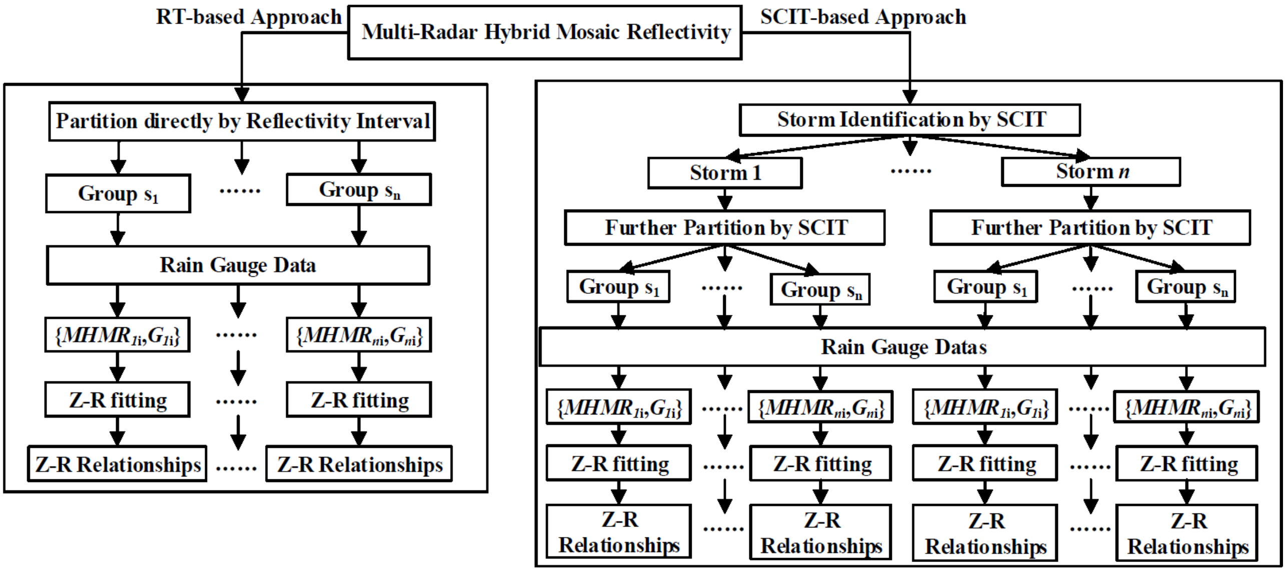

Fig. 6. Conceptual diagram of the RT and SCIT-based radar rainfall approaches.

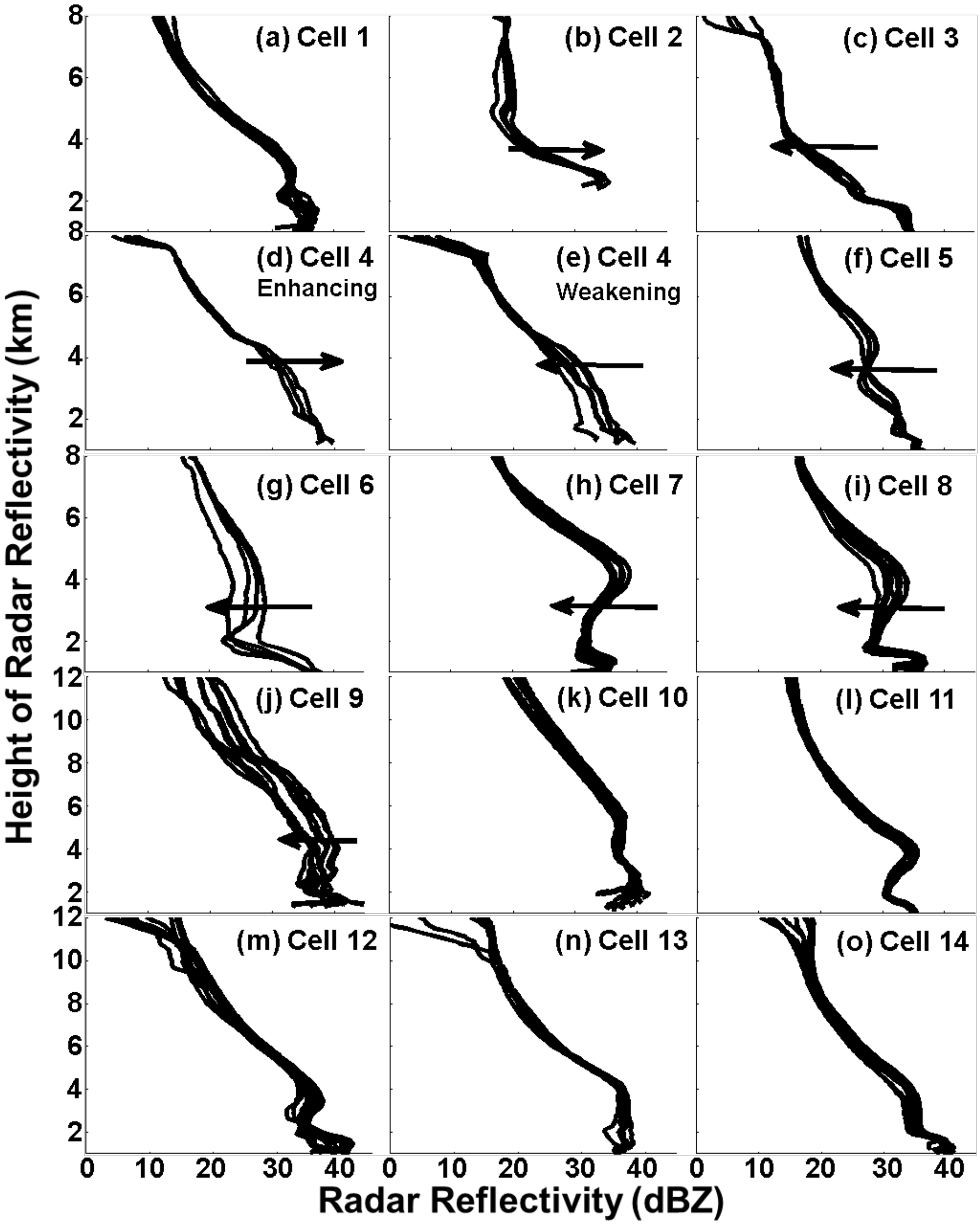

Fig. 7 Storm-scale VPR clusters for the 14 storm cells illustrated in Fig. 4 in 1-h span. The arrows denote the developing trends of the VPRs. In particularly, cell 4 was gradually enhanced in (d) but weakened in (e). The number of VPR profiles for each storm cell is listed in Table 3.

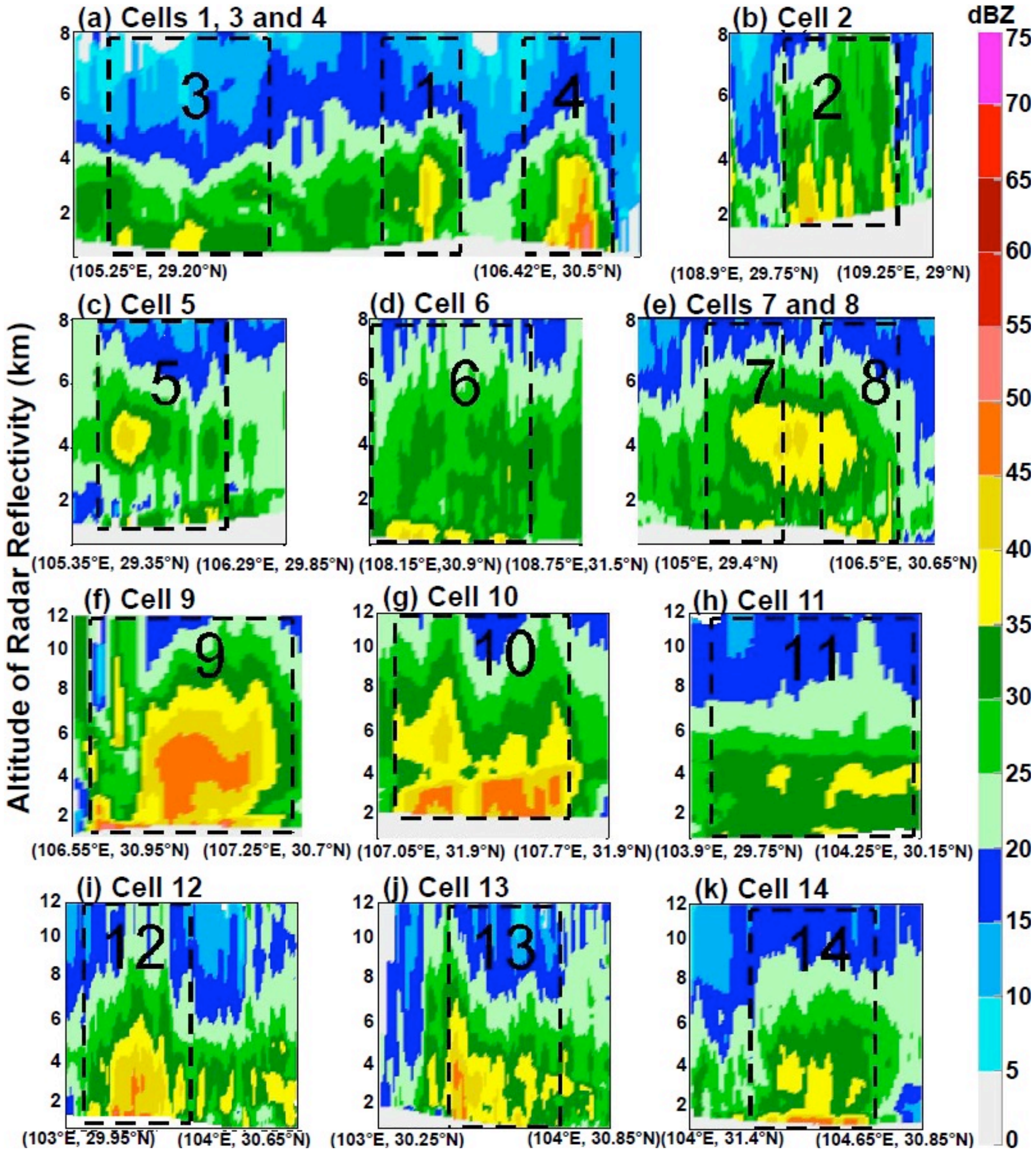

Fig. 8. Vertical profiles of reflectivity for the 14 storm cells indicated in Fig. 4. (a) Cells 1, 3, and 4; (b) cell 2; (c) cell 5; (d) cell 6; (e) cells 7 and 8; (f) cell 9; (g) cell 10; (h) cell 11; (i) cell 12; (j) cell 13; and (k) cell 14. The starting and ending locations (Lat/Long) of each cross section line are marked on the x-axes, and the vertical columns of the storm cells are denoted by the dashed-lines. More information about these 14 storm cells can be found in Table 3.

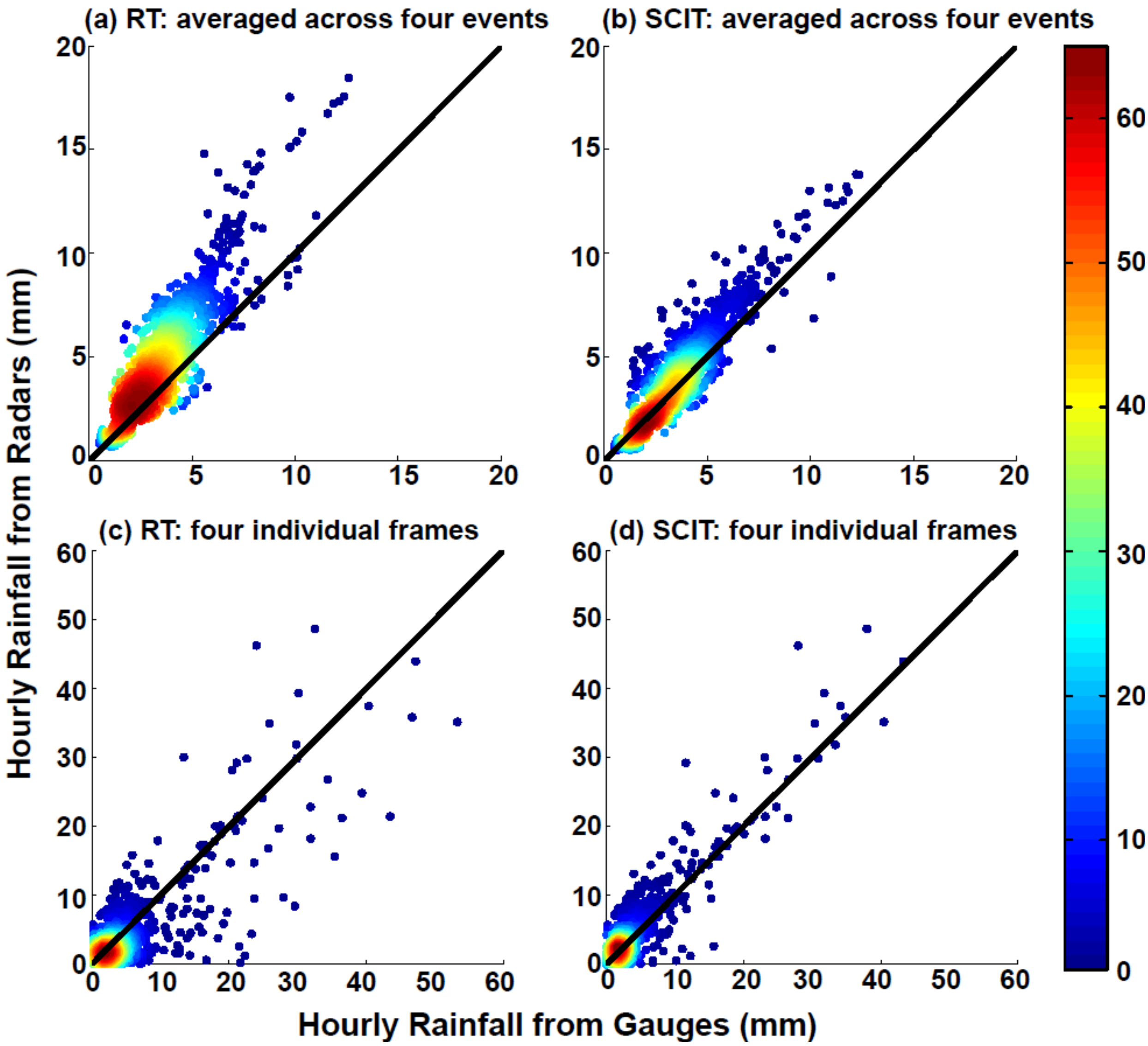

Fig. 9. Scatter plots of radar-derived hourly rainfall versus gauge observations. (a) and (b) are averaged RT- and SCIT-based rainfall estimates across four events; (c) and (d) are RT- and SCIT-based rainfall estimates for four time frames at 0230 UTC 28 Mar 2014, 2000 UTC 18 May 2014, 1200 UTC 02 Jun 2014, and 0100 UTC 31 Jul 2014.

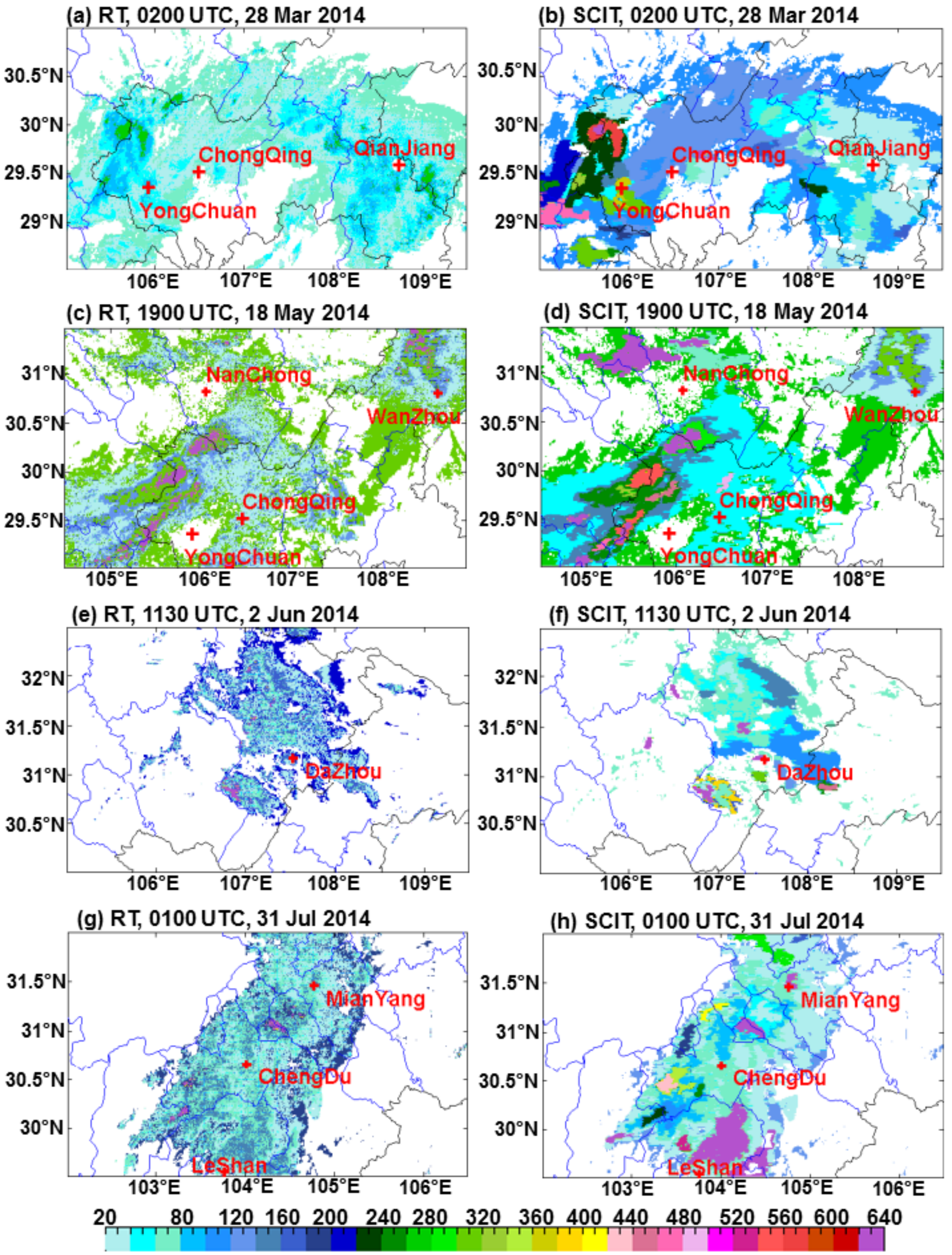

Fig. 10. Spatial distribution of the *Z*–*R* relationships [*b* = 1.6, the color represents value of coefficient *A*]. (a), (c), (e), and (g) are for the RT-based approach at 0200 UTC 28 Mar 2014, 1900 UTC 18 May 2014, 1130 UTC 2 Jun 2014, and 0100 UTC 31 Jul 2014, respectively. (b), (d), (f), and (h) are for the SCIT-based approach at the same time frames.